Efficient photodegradation of dye pollutants using a novel plasmonic AgCl microrods array and photo-optimized surface-enhanced Raman scattering

Yi-Feng Cheng[a], Qi Cao[b], Jie Zhang[a], Tong Wu[c], Renchao Che[a,*]

[a] *Laboratory of Advanced Materials, Department of Materials Science, Collaborative Innovation Center of Chemistry for Energy Materials, Fudan University, 2205#, Songhu road, 200438, Shanghai, China*
[b] *School of Engineering, The University of Tokyo, 7-3-1 Hongo, Bunkyo-ku, Tokyo 113-8656, Japan*
[c] *Dow Chemical (China) Investment Company Limited, 936#,Zhangheng Road, Zhangjiang Hi-Tech Park, Shanghai, 201303, China*

ARTICLE INFO

ABSTRACT

A novel arrayed AgCl micro-rods have *in situ* grown on an Ag foil successfully for the first time. The preparation process is consisted of two facile steps: (1) immersed oxidation and (2) directional ions exchange. The structure of the as-synthesized arrayed substrate has been characterized comprehensively, and the relevant growth mechanism is proposed. This highly aligned AgCl arrays show a remarkable visible-light-driven photocatalytic activity towards degrading 10^{-5} mol/L rhodamine 6G (R6G) aqueous solution. The ultra-stable catalytic performance of the plasmonic arrays was revealed by the recycled tests in the neutral and acidic conditions. Moreover, a facile SERS substrate based on the AgCl arrays was obtained with the optimal enhancement factor (EF) of $\sim 3.25 \times 10^{7}$, by directly putting the substrate under a Xe lamp in 7.5 min. Amazingly, the photo-optimized surface-enhanced Raman scattering (SERS) substrate still shows a stable activity for photodegrading R6G. The photocatalytic and SERS mechanism are proposed in this study.

© 2017 Published by Elsevier B.V.

1. Introduction

Semiconducting photocatalysis is one of the potentially promising strategies towards handling the current energy and environmental problems, such as splitting water, treating waste water and air pollution [1–5]. Therefore, intensive enthusiasms have been devoted to develop semiconducting micro/nano-materials, which aimed to solving the energy shortage and environmental pollution [6–11]. However, the classical semiconductors, ZnO [12–14], TiO$_2$ [15–17] and etc., are generally worked under the ultraviolet light due to their relative large band gaps [18]. Besides, many oxide semiconductors, such as Fe$_2$O$_3$ and ZnO, are not durably in the acidic condition owing to the property of acid dissolution. Therefore, it is worth to develop a visible-light-driven photocatalytic system to adapt to the complex environment in practical applications. Diverse nano-modified technologies have been successfully adopted to tune the responded wavelength of the semiconductor within the visible light range. Simultaneously, the modified

materials have shown efficient catalytic activities by the rational methods [19–21], such as doping element [22,23], loading novel metal [24–26], constructing heterojunction and controlling morphology [27–31]. However, the modified strategies inevitably increase the costs and complexity of the preparation processes, causing these photocatalysts less appealing to widespread commercial application [32].

Generally, a potentially promising photocatalyst can be evaluated from two necessary factors: the activity and durability [33]. The Ag-based semiconductors, such as AgCl [34], AgBr [35], AgI [36], Ag$_3$PO$_4$ [37] and Ag$_2$O [38], have been frequently explored as the typical visible-light-driven photocatalysts [39–41]. Especially, Huang's group revealed the plasmonic Ag@AgCl shows a stable visible-light-driven photocatalytic activity over the N-doped TiO$_2$ with several times [42]. Additionally, other novel designs of Ag-based semiconductors were emerged constantly with the visible-light-driven catalytic activities [43–47]. For instance, the high-index faceted AgCl polyhedra with different geometries have been reported that the exposure of the active crystal plane largely affects the resultant photocatalytic activities of the AgCl [48]. Therefore, it is effective and challenging to control the active facets specifically exposed on the surface of AgCl crystal for improv-

ing photocatalysis. Besides, the Ag/AgCl plasmonic photocatalytic cubes had been respectively prepared by two novel methods: the sonochemical approach [49] and one-pot laser irradiation [50]. Accordingly, these AgCl plasmonic photocatalysts generally take a regular geometries, such as cube and polyhedron, because of their intrinsic lattice characters ($a = b = c$ and $\alpha = \beta = \gamma = 90°$). Therefore, it is difficult to prepare an AgCl crystal with a relative large aspect ratio, such as the rod-like, due to the rapid growth kinetics of AgCl crystals and the isotropy along the direction of a, b and c-axis [49]. Furthermore, the well-aligned Ag_2S semiconductors had been in situ fabricated on the Ag foil, and this fabrication had successfully tuned the morphology of the Ag_2S to evolve from the nanoplates to the microtubes and microrods [51]. Moreover, the long AgBr nanowires had been successfully prepared on the Ag foil, exhibiting an excellent photocatalytic property [52]. Besides, Bi and his coworkers had synthesized the tetrahedral Ag_3PO_4 submicro-crystals on the Ag foil by a facile reaction at room temperature, and their product shows an efficient visible-light-driven photocatalytic performance [53]. However, the in situ growth of AgCl crystal on the Ag foil is rarely reported yet. Hence, the above synthetic methods inspire the rational strategy of in situ growing AgCl array on the Ag foil. Meanwhile, the development of a novel AgCl substrate is meaningful for the structural diversities and practical applications of the semiconductor. Additionally, AgCl is one of the photo-sensitive materials and the Ag^+ cations can receive the photogenerated electrons to convert into Ag (0) under photoirradiation [48,50,53]. The metallic Ag nanoparticles (NPs) have been shown a superior SERS performance, and the SERS is nowadays a well-established ultra-sensitive technique with the potential to detect molecules at the low concentrations ($<10^{-5}$ mol/L) [54]. Therefore, it is rewarding to explore the possibility that the Raman scattering enhancement collectively loads on the novel photocatalytic AgCl substrate by a photo-irradiation approach. Simultaneously, it is worthwhile to develop the potential multifunction of AgCl substrate based on photocatalysis and SERS.

Herein, we intend to design a novel AgCl micro-rods array with the remarkable visible-light-driven catalytic activity and stable recyclability in the neutral and acidic conditions. This novel AgCl array was firstly established through two steps. The smooth AgCl rod possesses the perfect crystallinity and ends up with a triangular pyramid tip. The triangular pyramid tip exposes three equivalent triangular facets indexed with the (111) plane. The AgCl micro-rod grows along the c-axis with a relative large aspect ratio. Moreover, this arrayed substrate costs 60 min in degrading above 98% R6G solution of 10^{-5} mol/L under the visible-light. This efficiency can be maintained after 500 min of the recycled degradations. Furthermore, the catalytic performance can be improved largely in presence of H^+ and Cl^- ions. The facial SERS substrate has been explored by directly photo-irradiating the AgCl array. The optimal Raman signal enhancement was obtained after the substrate being photo-irradiated for 7.5 min. The local surface phonon resonance (LSPR) mediated photocatalytic and SRES mechanisms have been proposed in this study. Discoveries from this study probably endow the substrate with the possibility to applicate in the natural environment protection and other novel devices.

2. Experimental section

2.1. Materials and chemicals

Silver foils (0.025 mm thick, annealed, 99.95%, Alfa Aesar), polyvinylpyrrolidone (PVP, K-30, AR, Sinopharm Chemical Reagent Company), sodium phosphate monobasic dihydrate ($NaH_2PO_4 \cdot 2H_2O$, AR, Sinopharm Chemical Reagent Company), hydrogen peroxide (30%, Sinopharm Chemical Reagent Company),

hydrochloric acid (36%, Sinopharm Chemical Reagent Company), sodium hydroxide (NaOH, AR, Sinopharm Chemical Reagent Company), sodium chloride (NaCl, AR, Sinopharm Chemical Reagent Company), rhodamine 6G (R6G, AR, Sinopharm Chemical Reagent Company), methyl orange (MO, AR, Sinopharm Chemical Reagent Company), acetone (AR, Sinopharm Chemical Reagent Company), ethylene glycol (EG, AR, Sinopharm Chemical Reagent Company), nitric acid (68%, Sinopharm Chemical Reagent Company), anhydrous ethanol (AR, Sinopharm Chemical Reagent Company) and anhydrous isopropanol (AR, Sinopharm Chemical Reagent Company) were used as received without further purification. All experiments were carried out in the laboratory atmosphere and the pure deionized water (DI water, Millipore) with the resistivity greater than 18.0 MΩ cm was used.

2.2. Preparation of AgCl micro-array

Firstly, a silver foil was cut into pieces (4×2 cm^2) and cleaned by dilute nitric acid solution, isopropanol, acetone, ethanol and water respectively. The cleaned Ag piece was first placed into the 6 mL mixed aqueous solution of NaH_2PO_4 (0.2 M) and PVP (0.6 M). Then 3 mL fresh H_2O_2 aqueous solution (30%) was added to the mixture drop by drop, and then the mixture was stayed at room temperature for about 12 h. Resultantly, the surface of the Ag piece was covered with a dark-yellow layer of Ag_3PO_4 [53]. The XRD pattern was seen in Fig. S1 (Supplementary materials). The dark-yellow piece was carefully cleaned by ethanol and water respectively. The EG (5 mL) and 36% hydrochloric acid (15 mL) were mixed together and loaded in a 50 mL Teflon-lined stainless-steel autoclave. Then one piece of the as-synthesized Ag_3PO_4 substrate was immersed into the mixture with an angle against the wall of the Teflon-liner. The autoclave was then heated to 150 °C, maintained for 5 h and then allowed to cool down to the room temperature. The eventually obtained light-brown-red foil was meticulously washed by water and ethanol for several times and dried naturally.

2.3. Photocatalysis test

In order to simplify the operations, all the tests were carried out in a quartz cuvette ($1 \times 1 \times 4$ cm, Jingke Optical Instrument, Yixing). Typically, a piece of substrate (about 0.5×3 cm, 26.2 mg) was cut from the as-obtained AgCl substrate and put into the quartz cuvette with an angle against the wall of the cuvette. Then 3 mL fresh R6G aqueous solution (10^{-5} mol/L, pH = 6.47) was transferred into the cuvette. The pH value was recorded by a pH meter (METTLEK TOLEDO, FE20) in laboratory atmosphere. To ensure the absorbance-desorption equilibrium between the R6G and AgCl substrate, this cuvette was kept in the dark for two hours before starting the photo-decomposing reaction. Finally, the quartz cuvette was exposed under a Xe lamp (PE300BF, 50 W, MICROSO-LAR300 system, Perfect-Light Company, Beijing) equipped with a UV cut-off filter ($\lambda > 400$ nm) at room temperature, and the lamp height (from the cuvette to the exit window) was preserved at 10 cm. Under the photo-control mode of MICROSOLAR300 system, the lamp current was fixed at 13.5 A which to ensure the light intensity near the cuvette was stabilized at about 92.74 mW/cm^2. The light intensity measured by a digital radiodetector (PM100D, THORLABS GmbH, Dachau Germany). The UV–vis absorbance spectra of the R6G solution were monitored simultaneously at selected time intervals. Additionally, three groups of fresh R6G solutions (10^{-5} mol/L) were respectively prepared by 0.1 M HCl, 0.1 M NaCl and 0.1 M NaOH aqueous solutions, traded as the controls and degraded in the same condition. The pH values of the three controls were 1.10, 6.51 and 12.73, respectively.

All the photocatalytic recyclability of AgCl substrates was examined by 5 cycles. Before entering a new cycle of photocatalytic

reaction, the substrate was recycled and then rinsed by ethanol and deionized water for several times. In every repeat photocatalytic test, all the measurement conditions were kept constantly.

2.4. Growth of Ag nanoparticles on the AgCl micro-array and the in situ measurements

The as-obtained AgCl substrate was directly placed under a bare Xe lamp (PE300BF, 50 W, 300 nm $\leq \lambda \leq$ 1100 nm, MICROSOLAR300, Perfect-Light Company, Beijing) with height of 10 cm from the exit window to the substrate. The energy distribution instruction of the lamp (PE300BF) was placed in Supplementary materials (Fig. S2). Under the photo-control mode of MICROSOLAR300 system, the lamp current was also fixed at 13.5 A and the light intensity near the substrate was stabilized at about 105.04 mW/cm^2. The UV–VIS spectra, XRD and SEM characterization of the substrate were respectively measured after the series of photo-irradiated times: 2.5 min, 5.0 min, 7.5 min, 10.0 min, 12.5 min, 15 min and 30 min. Meanwhile, the time-dependent SERS performances of the substrate were respectively examined after the photo-irradiations.

2.5. SERS measurements

Firstly, R6G aqueous solution (10^{-5} mol/L) of 10 μL was dropped onto an AgCl substrate after the photo-irradiation, and then the substrate was placed in dark for two hours. Then the substrate was dried at 60 °C for 0.5 h in a vacuum drying oven. Secondly, The Raman spectra were recorded from 20 random spots near the drop-casted center of the substrate. All the tests were used the identical instrumental settings. Specifically, the excitation source was the 785 nm laser and objective lens of 50 × /0.50 were used to focus the laser beam. The exposure time was set at 10 s and every resultant spectrum was accumulated three times. The laser power was maintained at 2.5 W (5% × 50 W) with an average spot size about 2 μm diameter in all acquisitions. Besides, the Raman signal intensities were averaged from the 20 spectra for final comparisons. Thirdly, the substrate was recycled by rinsing with deionized water and ethanol for several times. Then the clean and dry substrate was exposed under the Xe lamp again for next SERS detection until the accumulated photo-irradiation time of the substrate reaches 30 min.

2.6. Characterization

Powder X-ray diffraction (XRD) measurements were performed on an X-ray diffraction (D8-Advance, Bruker, Germany) equipped with Cu-Ka radiation (1.5406 Å). The scanning electron microscope (SEM) images were conducted on a field-emission SEM (FESEM, HITAICH, S-4800) worked at 1.0 kV. High-resolution transmission electron microscopy (HRTEM) analysis was carried on a field-emission TEM (FE-TEM, JEOL JEM-2100F, Japan) equipped with a post-column Gatan imaging filter system (GIF, Tridium 863, United States) working at 200 kV of the acceler-ation voltage. The TEM sample was prepared through scraping the AgCl substrates by a plastic tweezers in ethanol accompanied with sonication. Then the obtained-suspension was grinded in a mortar for several times. The UV–VIS absorption spectra of R6G solution were examined on an UV/VIS spectrometer (PerkinElmer, Lambda 35). The UV–VIS diffuse reflectance spectra of AgCl substrate were recorded on an UV–VIS–NIR spectrophotometer (UV–3600, Shimadzu, Japan). Room-temperature Raman spectra were collected utilizing a laser confocal Raman micro-spectrometer (inVia reflex, Renishaw, UK) equipped with a dual-head microscope (Leica DM-2500, Germany)
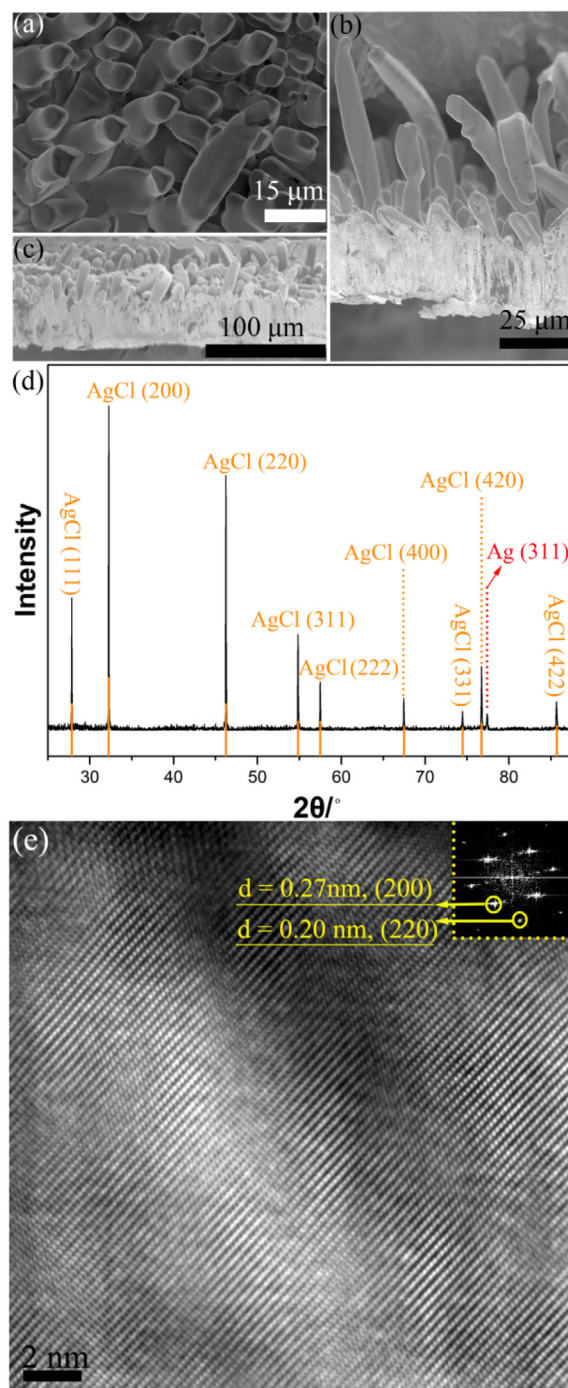

Fig. 1. The typical SEM images of the as-obtained AgCl array substrate: (a) top-view image; (b) and (c) side-view images at different magnifications. (d) XRD pattern of the as-prepared crystalline AgCl array. (e) HRTEM image showing the crystalline nature of the AgCl with an FFT (Fast Fourier Transform) pattern inset transformed from the whole HRTEM area of the picture.

3. Results and discussion

3.1. Material characterizations and grown mechanism

The SEM images of AgCl substrate were characterized with different magnifications and from different angles (Fig. 1a–c). The AgCl microrods stand upright on the substrate basically and end up with the triangular pyramid tips. The smooth microrods show a relatively uniform distribution of diameters (7–9 μm). The lengths
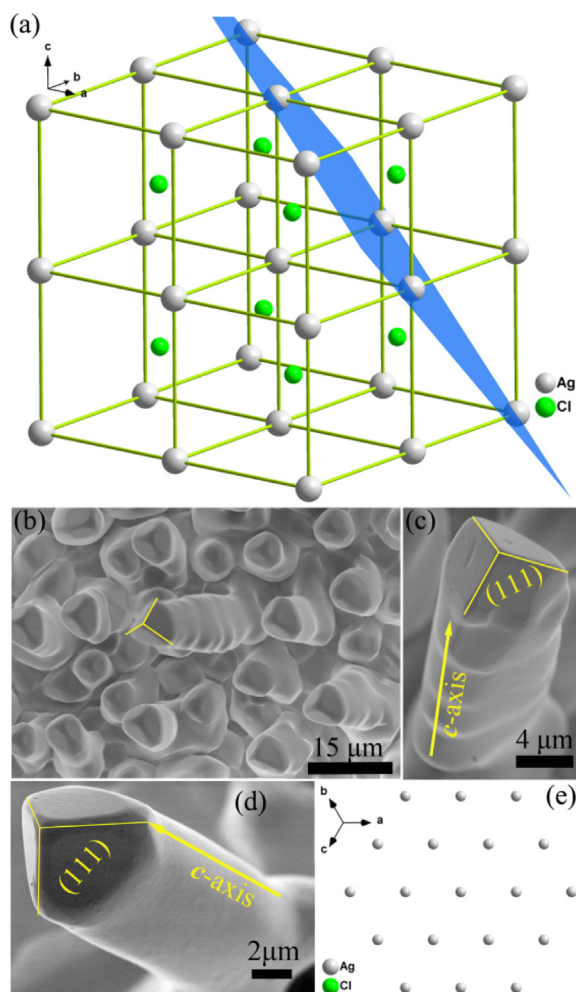
Fig. 2. (a) The body-centered structure of the cubic AgCl lattice. The lattice plane of (111) indicated by the blue color. (b) The typical SEM image of the AgCl microrods with the triangular pyramid tips from the top view; (c) and (d) the enlarged SEM images of the AgCl microrod with a triangular pyramid tip from different angles. (e) The atomic arrangement model of the cubic AgCl crystal by viewing along [111]. (For interpretation of the references to colour in this figure legend, the reader is referred to the web version of this article.)

of the microrods are not so uniform and some of the longer ones are curved (Fig. 1b and c). The relatively flat surface of the fresh Ag foil (Fig. S3, Supplementary materials) further demonstrates the *in situ* grown trait of the AgCl microrods. The characteristic peaks of the XRD pattern (Fig. 1d) fit exactly to the body-centered cubic AgCl (Fm-3m, JCPDS No. 31-1238) with the lattice parameters $a = b = c = 5.5491$ Å and $\alpha = \beta = \lambda = 90°$. The high intensities and sharp diffraction peaks reveal an excellent crystallinity of the AgCl crystal. Additionally, there is a weak peak of Ag (311) (Fm-3m, JCPDS No. 04-0783) indicated by the red color, which can be assigned to the residual metallic Ag of the substrate. Except for the signal of the metallic Ag, no other impurity can be found in the XRD data. Moreover, the HRTEM analysis (Fig. 1e) exhibits crystallinity nature of the microrods. The quadrilateral diffraction pattern of the FFT pattern is further coincidence with the pure cubic AgCl phase. The measured distances of the lattice spacing, 0.27 and 0.20 nm, could be assigned to the (200) and (220) planes respectively.

The preferably growth orientation of the AgCl microrod could be concluded from the co-relevance of the relative high and sharp peaks of (200) and (220) (Fig. 1d). Moreover, the crystal orientations of (200) and (220) are both parallel to the *c*-axis by analyzing the cubic unit cell of AgCl (Fig. 2a). Therefore, the radial direction

of the AgCl microrod could be assigned to the *c*-axis preliminarily [55]. Besides, the diffraction intensity of (111) plane is only weaker than that of (200) and (220) (Fig. 1d). Hence, the (111) plane has a sufficient exposure in the AgCl crystal. Furthermore, triangular pyramid tip of the AgCl microrod possesses three equilateral triangle facets. Thus the equivalent triangle planes could be indexed to (111) (Fig. 2b–d) from the feature of the cubic AgCl unit cell (Fig. 2a) [53]. Three (111) facets together terminate a microrod, which corroborates pervious sequitur that AgCl microrod grows along the *c*-axis. Interestingly, the atoms arrangement of the (111) plane reveals that this crystal plane only contains Ag atoms (Fig. 2e). The (111) plane enriched with Ag atom is a facilitated factor of the photocatalytic activity [48,53].

The AgCl microrod is able to break the restriction of the isotropy in the direction of *a*, *b* and *c*-axis. It could be explained by follows. Firstly, the growth of the AgCl crystal derives from the directional ions exchange between the Cl$^-$ and PO$_4^{3-}$ ions. The Cl$^-$ ions come from the aqueous solution, while the PO$_4^{3-}$ ions originate from the precursor of Ag$_3$PO$_4$ substrate. Although the Cl$^-$ ions have abundant diffusion directions in solution, the *in situ* reaction determines the substrate is the sole source of PO$_4^{3-}$ ions. Therefore, the directional ions exchange largely decreases the possibility that the crystal grows along multiple orientations. Secondly, the precursor of the tetrahedral Ag$_3$PO$_4$ substrate probably decides the crystal orientation of the resultant AgCl. Because the Ag$_3$PO$_4$ have the similar cubic crystal parameters ($a = b = c$ and $\alpha = \beta = \lambda = 90°$) to the AgCl crystal (Fig. S1). Meanwhile, the three equivalent (111) facets of the tetrahedral Ag$_3$PO$_4$ crystal reveal the *c*-axis is the axis-orientation of the tetrahedron [53]. A compared substrate was directly prepared using a cleaned Ag pieces to replace the precursor of the Ag$_3$PO$_4$ substrate (Fig. S4). The different SEM image and XRD pattern prove the precursor of Ag$_3$PO$_4$ substrate affects the preferably growth direction of the resultant AgCl crystal.

3.2. Photocatalytic performance

The photocatalytic activity of the AgCl substrate has been evaluated through decomposing R6G under visible light irradiation ($\lambda > 400$ nm). In dark, the time-dependent concentration changes (Fig. S5a) caused by the absorbance reveals the absorbance capacity of the AgCl array is very weak and the light irradiation is the necessary factor to starting the catalytic reaction. The representative UV–vis absorption spectra were used to monitor the kinetics of photodegrading R6G aqueous solution (10^{-5} mol/L, solvent: pure water) (Fig. 3a). The initial absorption spectrum of R6G displays a strong peak centered at about 527 nm (the black curve in Fig. 3a). In presence of the AgCl substrate, the absorption intensity of R6G solution was decreased gradually under the visible-light irradiation. Finally, the characteristic absorption peak of the R6G was weakened to invisibility at 60 min. To examine the stability of the photocatalytic performance in the AgCl substrate, the test of degrading R6G had been repeated for 5 cycles in the identical conditions (Fig. 3b). The efficiency can be maintained over 98%. Interestingly, the methyl orange (MO) aqueous solution (10^{-5} mol/L, solvent: pure water) can be degraded 99% in 40 min by continually using the recycled substrate (Fig. S6a). Furthermore, the photocatalytic performance of the recycled substrate is still stable and maintained above 97% in degradation of MO (Fig. S6a). After the total 500 min of the photocatalytic reactions, the recycled substrate still shows an efficient photocatalytic activity for decomposing 98% R6G in 60 min (Fig. S7). This stable and efficient photocatalytic activity of AgCl array is superior to the Ag$_2$S array [56] which respectively degrades the R6G and MO solution (10^{-6} mol/L) in 140 and 60 min.

Since the photo-sensitivity of the AgCl materials, the recycled AgCl substrate was examined by the SEM after the total 500 min of photodegradation (Fig. 4). The irregular pits and sporadic par-
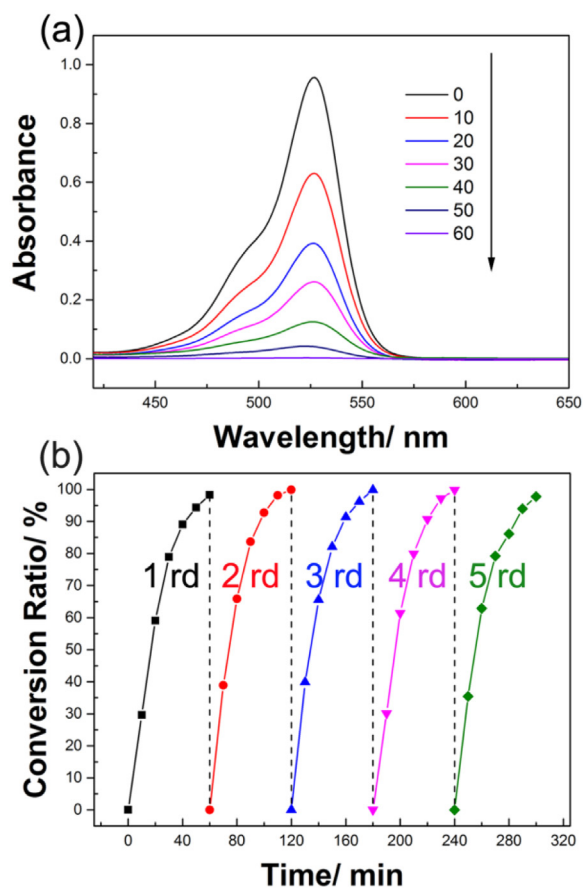
Fig. 3. (a) Under illumination of the visible light, time-dependent absorbance spectra of the R6G aqueous solution in the presence of AgCl substrate. (b) The recyclability of the AgCl substrate in photodegrading R6G.

Fig. 5. (a) The XRD pattern of the recycled AgCl substrate after 500 min of photodegradation test. (b) The ultraviolet-visible diffusive absorption spectra of the AgCl substrate before/after 500 min of photodegradation test.

ticles were found on the surface of the rod. Moreover, the weak diffraction peak of Ag (111) was detected in the XRD pattern of the recycled substrate (Fig. 5a). Besides, the diffraction intensity of Ag (311) increased slightly by comparing with that of fresh sub-
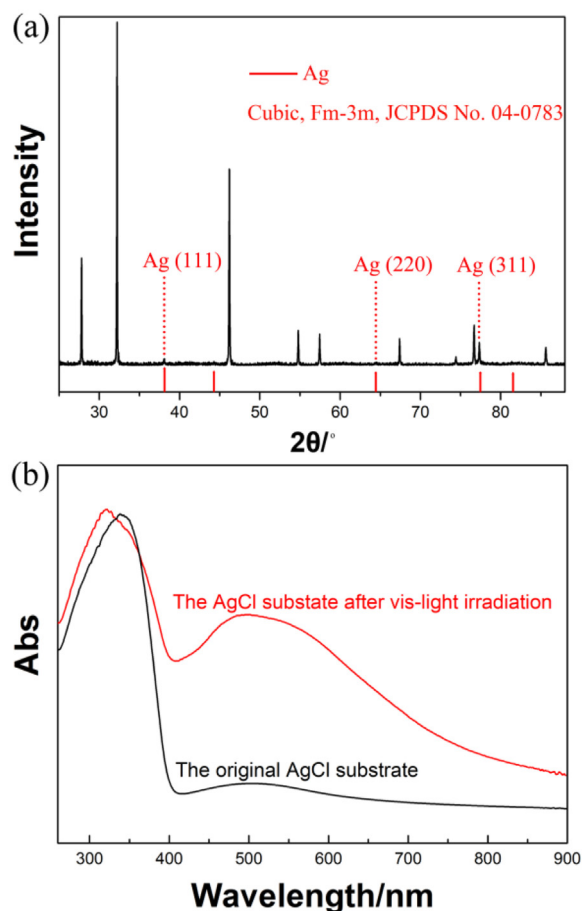
strate. Except for the changes in diffraction signals of metallic Ag, the peaks of AgCl do not occur any visible alterations. Accordingly, these changes can be attributed to the reduction of the Ag$^+$ cation
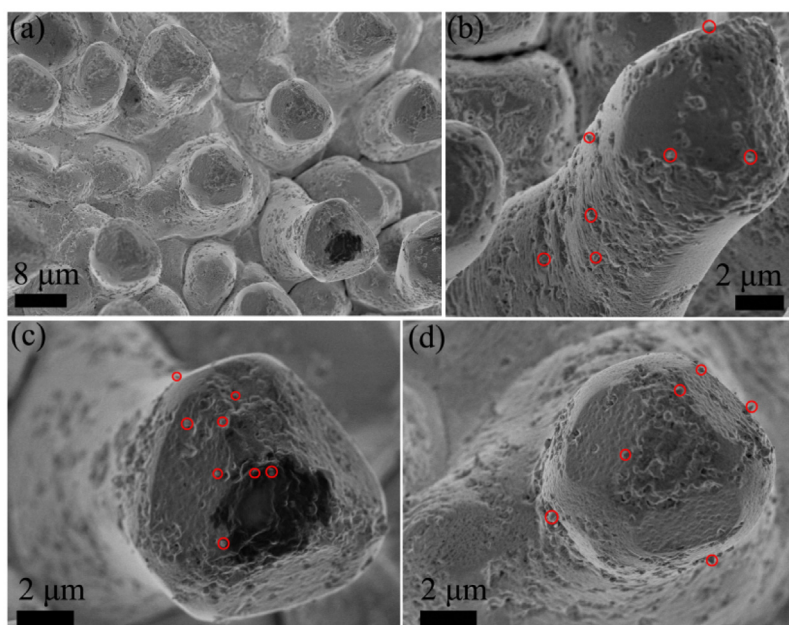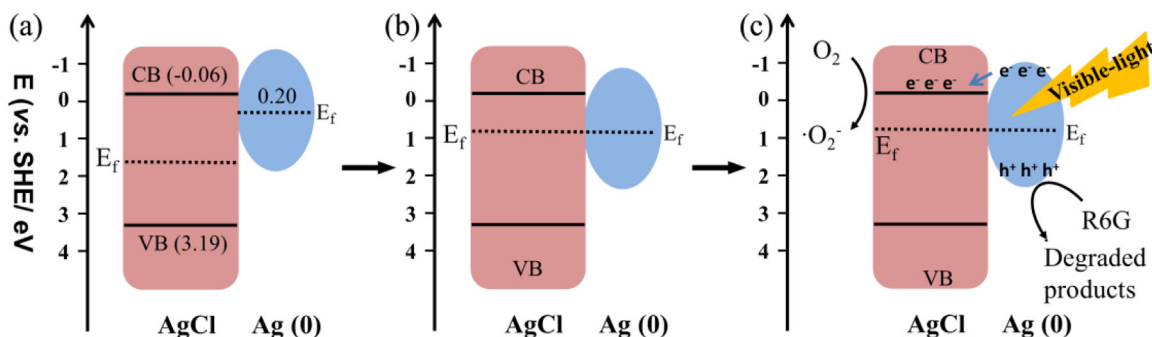

Fig. 4. (a–d) Typical SEM images of the AgCl substrate after 500 min of photodegradation test.

Fig. 6. Schematic illustration of the possible photocatalytic mechanism for arrayed AgCl crystal under visible light.

by the photogenerated electrons ($E^{\theta}_{Ag+/Ag}$ = 0.8 eV) [53]. Hence, the random grains anchored on the AgCl rod (Fig. 4) could be considered as Ag NPs. Furthermore, the strong absorption (about 340 nm) of the fresh AgCl substrate (Fig. 5b) is consistent to the indirect band gap energy (3.25 eV, ~380 nm) [57]. While the weak absorption (about 504 nm) could be caused by the trace of Ag NPs derived from the AgCl crystal under the irradiation of the weak environment light during the material preparation, storage or measurement [48]. However, the Ag absorption band (Fig. 5b) of the recycled substrate was changed in absorption intensity, absorption site and bandwidth. The results reveal that the sizes and quantity of the Ag NPs are increased on the AgCl substrate during the photodegradation. Besides, a slight enhancement and blue-shift were found in characteristic AgCl absorption band, compared with the spectrum of the fresh substrate. The photo-reduction of Ag$^+$ cations causes the atom vacancies on the surface of AgCl crystals [53], which probably accounts for the changes in AgCl band [55]. Although the surface of AgCl crystal experienced the photo-corrosion during the degradation, the mass of the AgCl is higher than the organic dye in this simply reaction system. Meanwhile, since the large band gap, the low photo-reduction rate of AgCl is not sufficient to cause a significant catalytic performance loss under the visible light. Therefore, the basic micro-arrayed structure of the substrate is still maintained. Accordingly, the stable degradation efficiency still demonstrates the AgCl array as an efficient photocatalytic substrate.

3.3. Photodegradation mechanism

It is obvious that AgCl semiconductor cannot be directly excited by the visible-light (λ > 400 nm) due to the largely indirect and direct band gap (3.25 eV and 5.15 eV) [57]. The relative weak absorption of the fresh AgCl substrate at about 504 nm (Fig. 5b) proves the Ag (0), which reduced by the environmental light, exhibits the localized surface plasmon resonance (SPR). Furthermore, the SPR effect of Ag (0) will be increased with the photo-irradiation due to the photo-reduction. Therefore, it is probably a SPR-mediated mechanism in this visible-light-driven photocatalysis. Specifically, because the Fermi level of Ag (0) is more negative than that of AgCl and locates between the valence and conduction bands of AgCl (Fig. 6a) [50]. The AgCl anchored with the Ag (0) leads to forming a Schottky barrier in the hybrid system. Therefore, the electrons will transfer from the Fermi level of Ag (0) to that of AgCl, until an equilibrated Fermi energy level is established between AgCl and Ag (0) (Fig. 6b) [58]. During visible-light irradiation, Ag (0) generates plasmonic electrons and holes due to SPR effect. As a result the Fermi energy level of Ag (0) will be further increased to above the conduction band of AgCl [50]. Hence, the plasmonic electrons can be injected into the AgCl conduction band by SPR effect (Fig. 6c) [50,58,59]. The injected electrons can trap with molecules and ions in surrounding to yield oxidative species,

such as ·O$_2^-$, while according to the report of Zhang's group [60], the plamonic hole (h$^+$) leaved in Ag (0) could directly react with R6G to generate the degraded product. It is said that the direct hole transfer is the major oxidative species to degrade the dye in the plasmonic AgCl/Ag catalyst. Moreover, the Ag (0) helps to facilitate the electron−hole separation, which subsequently promotes the formation of reactive species in photodegradation [48]. Additionally, the photo-reduced Ag NPs probably cause the atom vacancies on the surface of AgCl, and thus provide the photocatalytic active sites to degrade the dye [53,61]. Therefore, the increase of the active sites probably results in the stable photocatalytic activity of the AgCl array during the degradation. Besides, in the neutral condition, the weak absorbance between AgCl array and R6G (Fig. S5) reveals the sensitization of R6G may contribute an assistance to apply the visible light.

3.4. Effects of HCl, NaCl, NaOH on the R6G photodegradation

The photocatalytic performance of the AgCl substrate was also respectively evaluated by degrading three groups of R6G solutions (10^{-5} mol/L) with different additives: HCl, NaCl and NaOH, and the concentrations of each additive are 0.1 M. In dark, the weak absorbance between R6G and fresh AgCl (Fig. S5 b–d) indicates the light is the necessary factor in the catalytic reaction. Under the visible light, the AgCl array respectively spends 25, 50 and 80 min to catalyze the R6G solution (10^{-5} mol/L) with adding HCl, NaCl and NaOH (Fig. S8). The degradation rate of AgCl array was improved by adding with HCl and NaCl (Fig. 7a), but decreased by adding with NaOH. The linear plots of $-\ln(C_t/C_0)$ versus time (Fig. 7b) confirms the psreudo-first order reaction kinetics in the photodegradations [50] and the kinetic parameters (Table 1) indicate V(HCl) > V(NaCl) > V(pure water) > V(NaOH). Additionally, the catalytic efficiencies of the AgCl substrate stabilize at 97%~ in 0.1 M HCl and NaCl solution (Fig. S9 a–b). However, the catalytic performance of AgCl substrate shows a slightly loss in the 0.1 M NaOH (Fig. S9c), which the efficiency decreases from 90% to 86%.

The significant influences of the additives (HCl, NaCl and NaOH) on the photocatalytic performance of the AgCl array can be explained as follows. Firstly, a new absorption at 415 nm is gradually enhanced during the R6G photodegradation in the 0.1 M NaOH solution (Fig. S8c), while this absorption is not found in the R6G

Table 1
Summary for the Fitted Pseudo-First-Order Kinetic Rate Parameter (k), Kinetics Equations and the Corresponding Adjusted Regression Coefficients ($Adj.$-R^2).

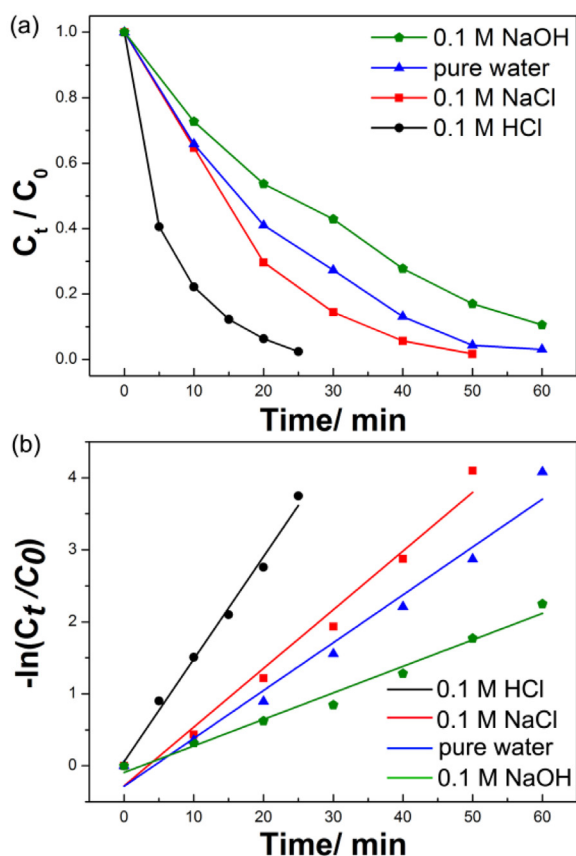| Additives	k (min^{-1})	Kinetics Equations	$Adj.$-R^2
HCl	0.1423	$y = 0.1423x + 0.05757$	0.99616
NaCl	0.0815	$y = 0.0815x - 0.27812$	0.98890
−	0.0664	$y = 0.0664x - 0.28392$	0.98709
NaOH	0.0368	$y = 0.0368x + 0.03683$	0.99136

Fig. 7. (a) Time-dependent degradation efficiencies of R6G solutions with different additives (b) The pseudo-first-order kinetic rate plots of R6G solutions with different additives.

degradation added with HCl and NaCl (Fig. S8 a and b). It proves that the photoxidation modes of R6G in the low pH (acidic and neutral) environments are quite different from that in alkaline environment. In details, the positive hole (h^+) is the direct oxidation species for R6G molecules in the acidic and neutral environments. However, in the 0.1 M NaOH solution, the positive hole (h^+) could inevitably react with the abundant OH^- ions to yield the hydroxyl radical ($^\bullet$OH). Therefore, in the strong alkaline solution, the hydroxyl radical ($^\bullet$OH) is probably the major oxidation species to degrade the dye [62]. Consequently, the pH range determines the photoxidation mode of R6G, and the photoxidation mode greatly affects the photocatalytic rates. Furthermore, the acid pH is beneficial to transfer the photogenerated electrons due to formation of the strong surface complex bond on catalyst [62]. However, the surface complex bond is less remarkable in alkaline pH and even is inhibited in the pH range of 11–13, because the $^\bullet$OH is rapidly scavenged and has less opportunity to react with dyes at this higher pH value [62,63]. Secondly, because AgCl are easily photo-reduced, the surface of AgCl is terminated with Cl^- ions and thus usually carried with the negative charge [64]. Therefore, in 0.1 M NaOH solution, the Coulombic repulsion probably inhibits the reactants contact with the Ag/AgCl catalyst. Besides, the alkaline environment accelerates the photo-corrosion of AgCl (Fig. S10), which probably results in the excessive Ag NPs decrease the active sites for electrons and holes. Thirdly, the oxide species probably oxidizes parts of photo-reduced Ag (0) to Ag^+ under the visible light. Therefore, the Cl^- ions of the HCl and NaCl probably combine with the Ag^+ to regenerate the AgCl (s) which have the higher reactivity than original AgCl matrix [40]. Therefore, the NaCl also improves the catalytic performance of AgCl array. Summarily, according to the SEM images (Fig. S10), the efficient and stable catalytic performance of AgCl substrate in acidic

and neutral environment demonstrates an excellent photocatalytic AgCl substrate has a potential application in pH < 7.

3.5. Surface evolution of the arrayed AgCl substrate under photo-irradiation

Inspired by the photo-sensibility of AgCl crystal, the *in situ* growth of Ag NPs on the AgCl substrate was triggered by the direct irradiation from a Xe lamp (300 nm–1100 nm, light intensity stabilized at 105.04 mW) with a timing-record. The time-dependent surface evolutions of the typical arrayed substrate were observed by SEM at every 2.5 min interval (Fig. 8). The smooth surface of the fresh AgCl microrod (Fig. 8a) gradually became rough by anchoring with many small Ag (0) granules (Fig. 8b). Then these granules sustainedly drew the Ag^+ from the AgCl to receive the photogenerated electrons, thus increasing their sizes and quantity. Therefore, the distances gradually became small between the adjacent Ag NPs (Fig. 8b–h). Finally, the metallic layer of the Ag NPs turned into more thick and continuous on the substrate. The Low magnification SEM images showed the *in situ* surface evolution of the arrayed substrate under the Xe lamp (Fig. S11-S18). However, the interdistance in a pair of the adjacent Ag NPs is a significant factor of plasmonic coupling, which is closely related to enhancement of SRES [65]. Therefore, SRES performance depends sensitively on the density and size of Ag NPs distributed on the substrate. Moreover, the photo-irradiated time directly decides the density and size of Ag NPs. As a result, the irradiatied time can be traded as the indirect variable to evaluate the SERS performance of the Ag-AgCl substrate. Especially, this variable is more easily controlled, compared with using the chemical method to control the sizes and distances among metal particles.

The ultraviolet-visible diffusive absorption spectra were collected from the substrate during the photo-irradiation (Fig. 9a). Two apparent trends respectively appeared in the AgCl absorption band (260–400 nm) and Ag absorption band (400–800 nm). As for the AgCl band (Fig. 9a), the AgCl peaks of the substrate were blue-shifted to about 312 nm by the photo-irradiation, compared with the initial one. The blue-shift probably derives from the atom vacancies caused by photo-reducing the Ag^+ cations on the surface of the substrate. Besides, the gradual enhancement of AgCl absorption is probably resulted from the increase of the Ag NPs during the photo-irradiation [66]. As for Ag band (Fig. 9a), the absorption peaks of the Ag NPs (2.5–30 min) showed a large enhancement by comparing the initial one. The enhancement indicates numerous metallic Ag NPs were appeared and anchored on the substrate during the photo-irradiation. Meanwhile, the Ag band gradually blue-shifted a small distance and narrowed slightly with increasing the time of photo-irradiation. The trend of Ag band is similar to the Ag@TiO$_2$ system reported by Kamat's group [67], and it is said that the electron density of the Ag NPs is increased during photo-irradiation. Actually, the absorption of metal NPs is related to many factors. For instance, the LSPR (local surface phonon resonance) absorption is blue-shifted with the metal NPs who possessed more symmetric [68]. With the irradiation of Xe lamp, the Ag NPs basically evolved from the irregular geometries to the near nano-spheres with more symmetric (Fig. 8). Hence, the geometry evolution of Ag NPs is probably one of the reasons for blue-shifting the Ag band. Additionally, in the presence of a substrate, the multipolar plasmon resonances influence the LSPR of Ag NPs [68]. This influence mainly focuses on the multipolar coupling or local field effects induced by the substrate. Hence, the distance between the surficial Ag NPs largely affects LSPR wavelength of the upper Ag NPs, because this distance decides the intensity. Meanwhile, the inner AgCl substrate influences the LSPR through inducing the mode of the multi-polarization [68]. Therefore, the gradual thickening of the Ag layer will affect the plasmonic coupling among the Ag NPs and
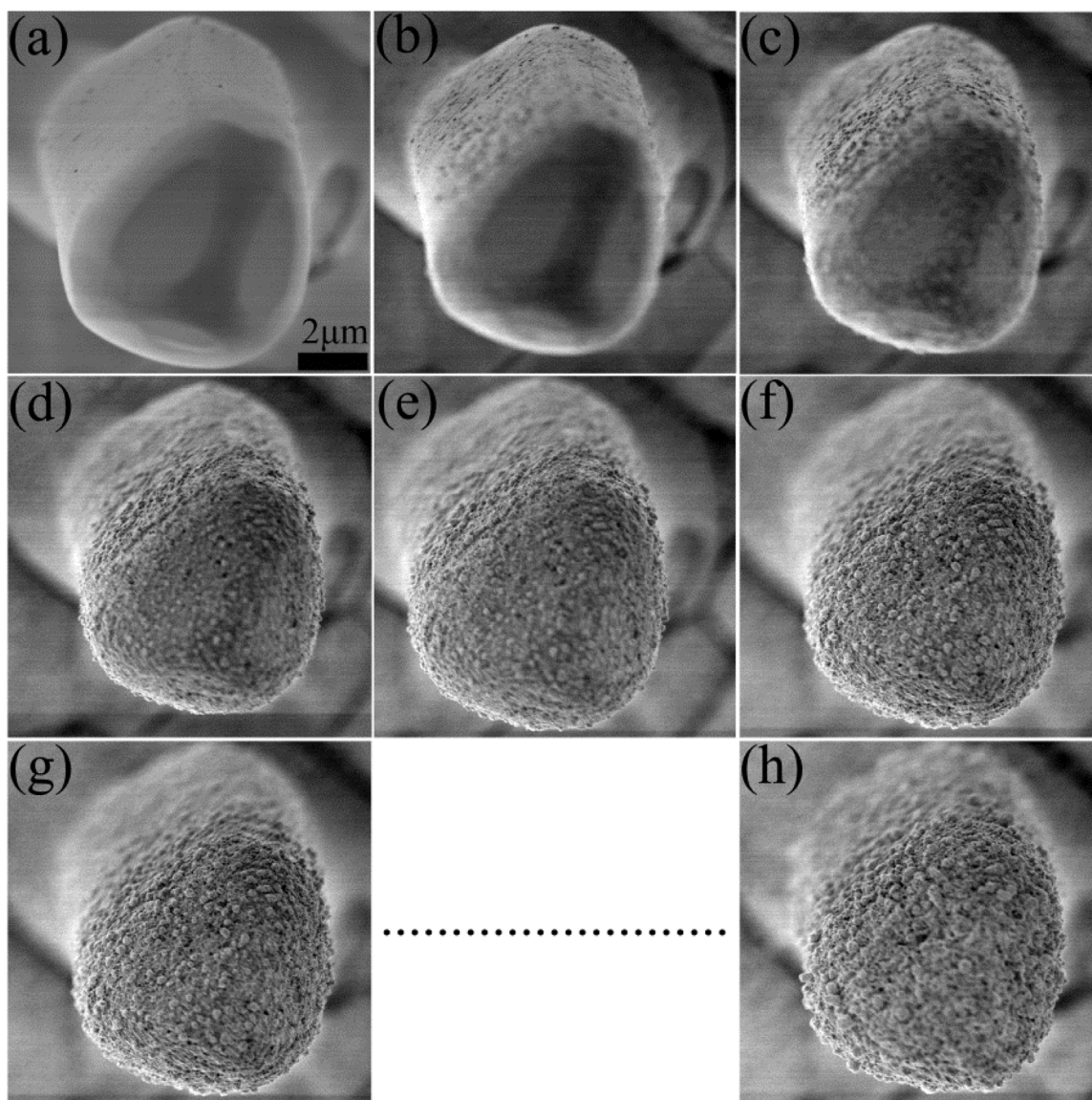
Fig. 8. The SEM images display the time-dependent surface evolution of the typical AgCl microrod under a bare Xe lamp: (a) 0 min; (b) 2.5 min; (c) 5.0 min; (d) 7.5 min; (e) 10 min; (f) 12.5 min; (g) 15 min and the last (h) 30 min.

dominate the multi-polarization. In specific, the LSPR wavelength of Ag NPs is blue-shifted with increasing the distance in an effective range [68]. Furthermore, the dipolar mode affects the LSPR wavelength of the metal. When a polarization direction of the incident light is perpendicular to the axis of inter-particles, this polarization probably contributes a part of effects to blue-shift the Ag-band [65]. In summary, the evolution of the metallic Ag layer on the AgCl substrate unavoidably changes the multipolar coupling and electromagnetic interactions between Ag NP and Ag NP/AgCl substrate, meanwhile, these interactions are related to SERS performance closely [69,70].

The diffraction intensity of the Ag NPs gradually increases with prolonging the photo-irradiation (Fig. 9b), thus further confirming the above discussion. Besides, the intensity ratio of AgCl (111) to AgCl (220) shows an apparent rise at 30 min (h) by comparing with that of the initial XRD pattern (a). This rise probably reveals that a collapse occurs in the axial-direction of the microrod. Therefore, in order to preserve the structural feature of the substrate, the time of the strong photo-irradiation should not be exceeded 30 min.

3.6. SERS detection of R6G on the arrayed Ag-AgCl substrate

The SERS performances *vs* the photo-irradiating time of the AgCl substrate (Fig. 10A) were estimated by detecting R6G aqueous solution (10^{-5} mol/L). A laser of 785 nm was used as the excitation wavelength. The characteristic Raman peaks (Fig. 10A) of R6G were detected at about 612 cm^{-1} (P1), 1313 cm^{-1} (P2), 1364 cm^{-1} (P3) and 1513 cm^{-1} (P4) [55,71]. Obviously, the clearest and strongest SERS profile was obtained on the substrate with photo-irradiation of 7.5 min. Besides, the Raman spectra of the pure Ag-AgCl substrate were recorded at every photo-irradiating interval (Fig. S19). No Raman peaks were detected between 500–2000 cm^{-1}, which reveals all the SERS peaks are related to the R6G molecule. Meanwhile, the SERS examination of the fresh substrate (Fig. S20) illustrates the Raman enhancement mainly caused from the photo-reducing Ag NPs. Furthermore, the enhancement factors (EFs) of the corresponding SERS spectra have been calculated from the intensities of P1, P2, P3 and P4. The intensities of the peaks were averaged by the 20 spectra which acquired from 20 stochastic spots on one substrate (Fig. S21–S24). The detail calculation method had been
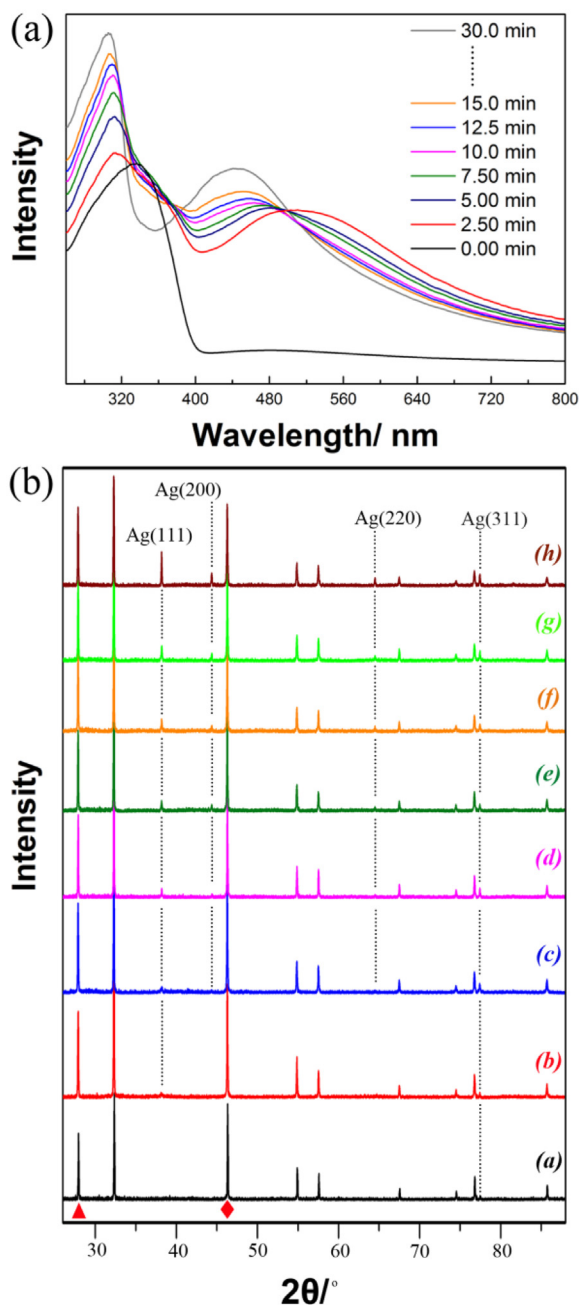
Fig. 9. (a) The UV–vis diffusive absorption spectra examine the *in situ* surface evolution of the AgCl substrate under the irradiation of a bare Xe lamp. (b) XRD patterns for the process of *in situ* growing Ag NPs on the subtrate by the photo-irradiation: *(a)* 0 min; *(b)* 2.5 min; *(c)* 5.0 min; *(d)* 7.5 min; *(e)* 10 min; *(f)* 12.5 min; *(g)* 15 min and the last *(h)* 30 min. The AgCl (111) and (220) are respectively indicated by red the triangle and quadrilateral. (For interpretation of the references to colour in this figure legend, the reader is referred to the web version of this article.)
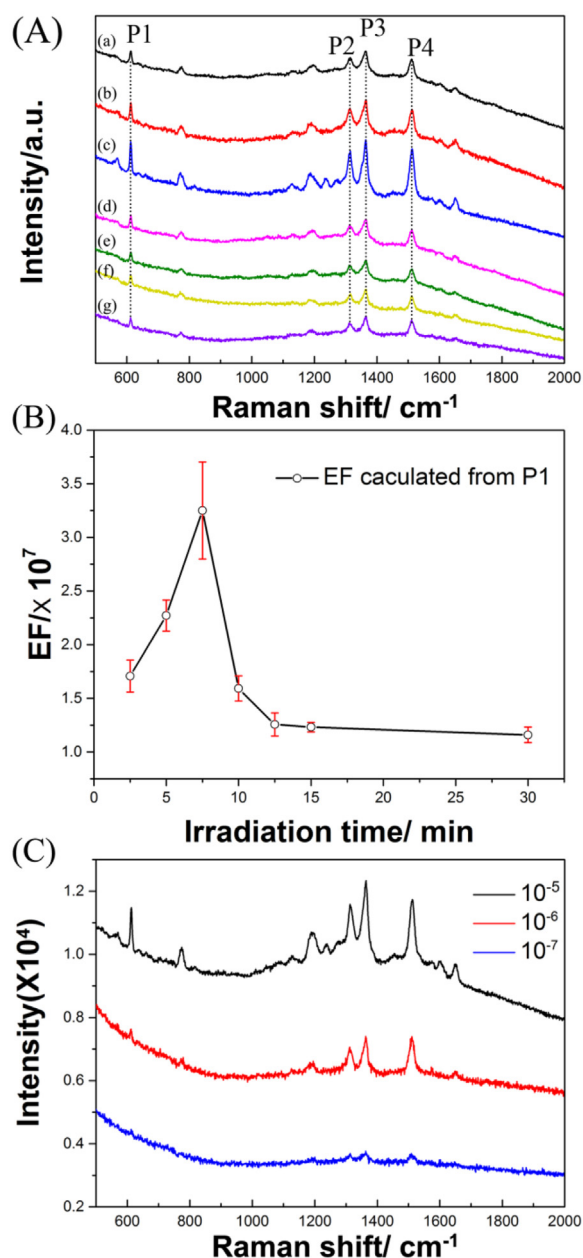
Fig. 10. (A) the Raman spectra of R6G solution (10^{-5} mol/L) deposited on the time-dependent Ag-AgCl substrate: (a) 2.5 min; (b) 5.0 min (c) 7.5 min; (d) 10.0 min; (e) 12.5 min; (f) 15.0 min and (g) 30.0 min. (B) The average EF values *vs* the irradiation time, which calculated from the P1. (C) The SERS spectra of the R6G solution with different concentrations on the photo-optimized AgCl substrate with 7.5 min of photo-irradiation.

provided in the Supplementary materials. The EF firstly increases with the photo-irradiating before 7.5 min (Fig. 10B), then shows a downtrend after 7.5 min and descends very gently after 12.5 min. The maximal EF appears at 7.5 min and the average value is about 3.25×10^7. The other EF profiles based on the P2, P3 and P4 (Fig. S21) display a similar trend *vs* the time of photo-irradiation. The EFs directly reflects the Raman enhancement effect of the substrate. Therefore, it reveals the substrate exhibits the optimal SERS performance with 7.5 min of photo-irradiation. The R6G solution of 10^{-6} and 10^{-7} mol/L were successfully detected on the optimal SERS substrate (Fig. 10C). Although the determination limit of the

optimal SERS substrate is incomparable to many excellent reports [72–74], the facial photo-irradiation provide a fast approach based on the photosensitive materials to detect the organic contaminants of one-millionth in wild. Additionally, although experiencing the strong photo-irradiation, the optimal Ag-AgCl substrate still exhibits a stable activity for photodegrading 97% R6G solution (10^{-5} mol/L, solvent: pure water) in 1 h (Fig. S21).

The SERS performance of the substrate depends sensitively on the time of photo-irradiation, because the time-dependent metallic Ag layer directly decides the size-dependent LSPR. However, the wavelength of LSPR is determined by the size and shape of metal NPs, which have been aforementioned. Besides, the inter-distance between two adjacent metal NPs reversely affects the intensity of the SERS signal [65]. The schematic diagram (Fig. 11) illustrates the
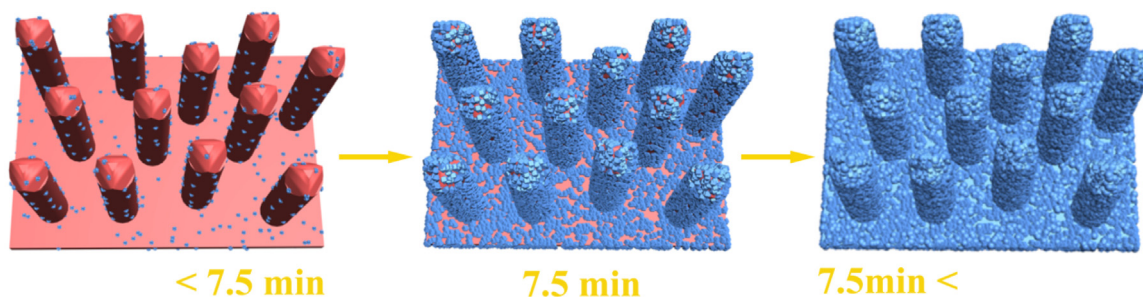
Fig. 11. Schematics illustrating the evolution of the metallic Ag layer on the arrayed AgCl substrate under the Xe lamp.

development in the density, size and geometry of the Ag NPs on the AgCl substrate. Firstly, density of the Ag NP increases largely by prolonging the photo-irradiation, leading to a blowout for the active vibration sites of the Ramon signals. Meanwhile, the inter-distances decrease progressively between the adjacent Ag NPs. Therefore, the distance-controlled plasmonic coupling of the inter-particles will probably enhance in the scattered electric field until these particles are in contact [65,75,76]. Accordingly, the active vibration sites and suitable plasmonic coupling could be the essential reasons for gradually amplifying SERS signal. Therefore, the substrate with optimal SERS performance can be ascribed to that the density, size and geometry of Ag NPs reaches the most suitable state for the SERS. Secondly, the Ag NPs continues to grow with the sustained photo-irradiation, resulting in the adjacent Ag NPs contact each other to form a metallic layer on the substrate. The upper Ag NPs can still be functioned as the active vibration sites for Ramon signals, but the coupling intensity is incomparable to the previous state. Hence, the enhancement effect decreases largely from 7.5 to 12.5 min. Besides, the upper Ag NPs keep away from the inner AgCl substrate due to thickening of Ag layer. When the thickness of the Ag layer exceed the radius of the upper Ag NPs, the multiple polarizations will be unsufficient [77,78]. As a result, the coupling intensity between Ag NPs and the active vibration sites of Raman can not be changed largely with the photo-irradiation. Therefore, the EF descends very gently after the photo-irradiating time over 12.5 min.

4. Conclusion

Summarily, the arrayed AgCl micro-rods have been successfully prepared for the first time *via* two facile steps: (1) immersion reaction at room temperature and (2) directional ions exchange by a hydrothermal process. The directional ions exchange breaks the isotropy restriction of cubic AgCl to obtain a rod-like crystal. The *c*-axis direction is preferred growth orientation of the AgCl micro-rod. Moreover, in acidic and neutral conditiona, the arrayed AgCl substrate displays a remarkable visible-light-driven photocatalytic activity as well as an ultra-stable recyclability in degrading R6G. Besides, the substrate exhibits an optimal SERS performance with the maximal EF of 3.25×10^7 after 7.5 min of photo-irradiation. The facial photo-irradiation inspires the possibility of using the photosensitive materials as a SERS substrate to fast detect the contaminants of one-millionth in the wild. A great potential of this substrate for environmental management lays the material foundation of future developing novel, efficient, integrated and multifunctional catalytic and sensing devices.

Acknowledgements

Appendix A. Supplementary data

Supplementary data associated with this article can be found, in the online version, at http://dx.doi.org/10.1016/j.apcatb.2017.05.021.

References

[1] M.R. Gao, Y.F. Xu, J. Jiang, S.H. Yu, Chem. Soc. Rev. 42 (2013) 2986–3017.
[2] X.B. Chen, S.H. Shen, L.J. Guo, S.S. Mao, Chem. Rev. 110 (2010) 6503–6570.
[3] X.F. Zhang, Y.N. Wang, B.S. Liu, Y.H. Sang, H. Liu, Appl. Catal. B: Environ. 202 (2017) 620–641.
[4] H.J. Yu, R. Shi, Y.F. Zhao, G.I.N. Waterhouse, L.Z. Wu, C.H. Tung, T.R. Zhang, Adv. Mater. 28 (2016) 9454–9477.
[5] X.Q. Xie, K. Kretschmer, G.X. Wang, Nanoscale 7 (2015) 13278–13292.
[6] K. Sekizawa, K. Maeda, K. Domen, K. Koike, O. Ishitani, J. Am. Chem. Soc. 135 (2013) 4596–4599.
[7] A. Kudo, Y. Miseki, Chem. Soc. Rev. 38 (2009) 253–278.
[8] H. Kisch, Angew. Chem. Int. Ed. 52 (2013) 812–847.
[9] Q. Guo, C.Y. Zhou, Z.B. Ma, Z.F. Ren, H.J. Fan, X.M. Yang, Chem. Soc. Rev. 45 (2016) 3701–3730.
[10] L.Q. Jing, W. Zhou, G.H. Tian, H.G. Fu, Chem. Soc. Rev. 42 (2013) 9509–9549.
[11] J.H. Kim, J.H. Kim, J. Am. Chem. Soc. 134 (2012) 17478–17481.
[12] L. Saikia, D. Bhuyan, M. Saikia, B. Malakar, D.K. Dutta, P. Sengupta, Appl. Catal. A: Gen. 490 (2015) 42–49.
[13] S. Thangavel, K. Krishnamoorthy, V. Krishnaswamy, N. Raju, S.J. Kim, G. Venugopal, J. Phys. Chem. C 119 (2015) 22057–22065.
[14] W.W. He, H.K. Kim, W.G. Wamer, D. Melka, J.H. Callahan, J.J. Yin, J. Am. Chem. Soc. 136 (2014) 750–757.
[15] R. Leary, A. Westwood, Carbon 49 (2011) 741–772.
[16] Z.P. Yan, X.X. Yu, Y.Y. Zhang, H.X. Jia, Z.J. Sun, P.W. Du, Appl. Catal. B: Envion. 160–161 (2014) 173–178.
[17] H. Xu, S.X. Ouyang, L.Q. Liu, P. Reunchan, N. Umezawa, J.H. Ye, Jinhua, Mater. Chem. A 2 (2014) 12642–12661.
[18] Y.Q. Qu, X.F. Duan, Chem. Soc. Rev. 42 (2013) 2568–2580.
[19] J.T. Zhang, Z.G. Xiong, X.S. Zhao, J. Mater. Chem. 21 (2011) 3634–3640.
[20] Y. Kofuji, Y. Isobe, H. Sakamoto, S. Ichikawa, T. Hirai, Y. Shiraishi, S. Tanaka, J. Am. Chem. Soc. 138 (2016) 10019–10025.
[21] R. Marschall, Adv. Funct. Mater. 24 (2014) 2421–2440.
[22] J.Z. Bloh, R. Dillert, D.W. Bahnemann, J. Phys. Chem. C 116 (2012) 25558–25562.
[23] Z. Dai, F. Qin, H.P. Zhao, J. Ding, Y.L. Liu, R. Chen, ACS Catal. 6 (2016) 3180–3192.
[24] N.S. Hondow, Y.H. Chou, K. Sader, R. Brydson, R.E. Douthwaite, J. Phys. Chem. C 114 (2010) 22758–22762.
[25] S.C. Han, L.F. Hu, N. Gao, A.A. Al-Ghamdi, X.S. Fang, Adv. Funct. Mater. 24 (2014) 3725–3733.
[26] X.G. Meng, L.Q. Liu, S.X. Ouyang, H. Xu, D.F. Wang, N.Q. Zhao, J.H. Ye, Adv. Mater. 28 (2016) 6781–6803.
[27] H.W. Huang, K. Xiao, Y. He, T.R. Zhang, F. Dong, X. Du, Y.H. Zhang, Appl. Catal. B: Envion. 199 (2016) 75–86.
[28] C. Terashima, R. Hishinuma, N. Roy, Y. Sugiyama, S.S. Latthe, K. Nakata, T. Kondo, M. Yuasa, A. Fujishima, ACS Appl. Mater. Interfaces 8 (2016) 1583–1588.
[29] H.W. Huang, K. Xiao, T.R. Zhang, F. Dong, Y.H. Zhang, Appl. Catal. B: Envion. 203 (2017), http://dx.doi.org/10.1016/j.apcatb.2016.10.082.
[30] D. Jiang, W.Z. Wang, L. Zhang, Y.L. Zheng, Z. Wang, ACS Catal. 5 (2015) 4851–4858.
[31] C.P. Athanasekou, S. Morales-Torres, V. Likodimos, G.E. Romanos, L.M. Pastrana-Martinez, P. Falaras, D.D. Dionysiou, J.L. Faria, J.L. Figueiredo, A.M.T. Silva, Appl. Catal. B Environ. 158–159 (2014) 361–372.

[32] H. Tong, S.H. Ouyang, Y.P. Bi, N. Umezawa, M. Oshikiri, J.H. Ye, Adv. Mater. 24 (2012) 229–251.
[33] X.G. Meng, L.Q. Liu, S.X. Ouyang, H. Xu, D.F. Wang, N.Q. Zhao, J.H. Ye, Adv. Mater. 28 (2016) 6781–6803.
[34] G.Q. Luo, X.J. Jiang, M.J. Li, Q. Shen, L.M. Zhang, H.G. Yu, ACS Appl. Mater. Interfaces 5 (2013) 2161–2168.
[35] H.G. Yu, L.L. Xu, P. Wang, X.F. Wang, J.G. Yu, Appl. Catal. B: Environ. 144 (2014) 75–82.
[36] C. Hu, T.W. Peng, X.X. Hu, Y.L. Nie, X.F. Zhou, J.H. Qu, H. He, J. Am. Chem. Soc. 132 (2010) 857–862.
[37] Z.G. Yi, J.H. Ye, N. Kikugawa, T. Kako, S.X. Ouyang, H. Stuart-Williams, H. Yang, J.H. Cao, W.J. Luo, Z.S. Li, Y. Liu, R.L. Withers, Nat. Mater. 9 (2010) 559–564.
[38] X.F. Wang, S.F. Li, H.G. Yu, J.G. Yu, S.W. Liu, Chem.-A Eur. J. 17 (2011) 7777–7780.
[39] J.G. Yu, G.P. Dai, B.B. Huang, J. Phys. Chem. C 113 (2009) 16394–16401.
[40] S. Garg, H.Y. Rong, C.J. Miller, T.D. Waite, J. Phys. Chem. C 120 (2016) 5988–5996.
[41] X.L. Ma, Y.X. Tang, H.J. Tao, Y.K. Lai, Y.Y. Zhang, X.R. Zhou, Z.S. Lv, Z.Q. Zhu, J. Tao, CrystEngComm 18 (2016) 3725–3733.
[42] P. Wang, B.B. Huang, X.Y. Qin, X.Y. Zhang, Y. Dai, J.Y. Wei, M.H. Whangbo, Angew. Chem. Int. Ed. 47 (2008) 7931–7933.
[43] R. Qiao, M.M. Mao, E.L. Hu, Y.J. Zhong, J.Q. Ning, Y. Hu, Inorg. Chem. 54 (2015) 9033–9039.
[44] H.M. Jia, W.W. He, W.G. Wamer, X.N. Han, B.B. Zhang, S. Zhang, Z. Zheng, Y. Xiang, J.J. Yin, J. Phys. Chem. C 118 (2014) 21447–21456.
[45] W. Zhao, Y.F. Liu, J.J. Liu, P. Chen, I.W. Chen, F.Q. Huang, J.H. Lin, J. M. Chem. A 1 (2013) 7942–7948.
[46] Q. Zhu, W.S. Wang, L. Lin, G.Q. Gao, H.L. Guo, H. Du, A.W. Xu, J. Phys. Chem. C 117 (2013) 5894–5900.
[47] J. Jiang, H. Li, L.Z. Zhang, Chem. − A Eur. J. 18 (2012) 6360–6369.
[48] H.B. Zhang, Y.G. Lu, H. Liu, J.Z. Fang, Nanoscale 7 (2015) 11591–11601.
[49] D.L. Chen, S.H. Yoo, Q.S. Huang, G. Ali, S.O. Cho, Chem. Eur. J. 18 (2012) 5192–5200.
[50] Z.Y. Lin, J. Xiao, J.H. Yan, P. Liu, L.H. Li, G.W. Yang, J. Mater. Chem. A 3 (2015) 7649–7658.
[51] D.P. Li, Z. Zheng, Y. Lei, F.L. Yang, S.X. Ge, Y.D. Zhang, B.J. Huang, Y.H. Gao, K.W. Wong, W.M. Lau, Chem. Eur. J. 17 (2011) 7694–7700.
[52] Y.P. Bi, J.H. Ye, Chem. Eur. J. 16 (2010) 10327–10331.
[53] H.Y. Hu, Z.B. Jiao, H.C. Yu, G.X. Lu, J.H. Ye, Y.P. Bi, J. Mater. Chem. A 1 (2013) 2387–2390.
[54] S. Schlücker, Angew. Chem. Int. Ed. 53 (2014) 4756–4795.
[55] S. Cong, Y.Y. Yuan, Z.G. Chen, J.Y. Hou, Y.L. Su, Y.Y. Zhang, L. Li, Q.G. Li, F.X. Geng, Z.Z. Zhao, Nat. Commun. 6 (2015) 7800–7806.
[56] Q. Cao, R.C. Che, N. Chen, Chem. Commun. 50 (2014) 4931–4933.
[57] S. Glaus, G. Calzaferri, Photochem. Photobiol. Sci. 2 (2003) 398–401.
[58] S.A. Ansari, M.M. Khan, M.O. Ansari, J. Lee, M.H. Cho, J. Phys. Chem. C 117 (2013) 27023–27030.
[59] J. Yan, W.Z. Zhou, H.Q. Tan, X.J. Feng, Y.H. Wang, Y.G. Li, CrystEngComm 18 (2016) 8762–8768.
[60] J. Jiang, L.Z. Zhang, Chem. Eur. J. 17 (2011) 3710–3717.
[61] X. Xiao, W.D. Zhang, J.Y. Yu, Y.J. Sun, Y.X. Zhang, F. Dong, Catal. Sci. Technol. 6 (2016) 5003–5010.
[62] I.K. Konstantinous, T.A. Albanis, Appl. Catal. B: Environ. 49 (2004) 1–14.
[63] J. Bandara, J.A. Mielczarski, J. Kiwi, Langmuir 15 (1999) 7680–7687.
[64] P. Wang, B.B. Huang, X.Y. Qin, X.Y. Zhang, Y. Dai, J.Y. Wei, M.H. Whangbo, Angew. Chem. Int. Ed. 47 (2008) 7931–7933.
[65] Q.M. Yu, P. Guan, D. Qin, G. Golden, P.M. Wallace, Nano Lett. 8 (2008) 1923–1928.
[66] S.C. Han, L.F. Hu, N. Gao, A.A. Al-Ghamdi, X.S. Fang, Adv. Funct. Mater. 24 (2014) 3725–3733.
[67] T. Hirakawa, P.V. Kamat, J. Am. Chem. Soc. 127 (2005) 3928–3934.
[68] C. Noguez, J. Phys. Chem. C 111 (2007) 3806–3819.
[69] R.A. Aílvarez-Puebla, J. Phys. Chem. Lett. 3 (2012) 857–866.
[70] A.R. Li, S.Z. Li, Nanoscale 6 (2014) 12921–12928.
[71] S. Mondal, U. Rana, S. Malik, ACS Appl. Mater. Interfaces 7 (2015) 10457–10465.
[72] W.H. Hsiao, H.Y. Chen, Y.C. Yang, Y.L. Chen, C.Y. Lee, H.T. Chiu, (3) (2011) 3280–3284.
[73] Q.Q. Ding, H.L. Liu, L.B. Yang, J.H. Liu, J. Mater. Chem. 22 (2012) 19932–19939.
[74] X.Y. Guo, Y.C. Fu, S.Y. Fu, H. Wang, T.Y. Yang, Y. Wen, H.F. Yang, Inorg. Chem. 53 (2014) 7227–7232.
[75] J.M. Nam, J.W. Oh, H. Lee, Y.D. Suh, Acc. Chem. Res. 10.1021/acs.accounts. 6b00409.
[76] J.H. Lee, M.H. You, G.H. Kim, J.M. Nam, Nano Lett. 14 (2014) 6217–6225.
[77] R. Wannemacher, A. Pack, M. Quinten, Resonant absorption and scattering in evanescent fields, Appl. Phys. B 68 (1999) 225–232.
[78] N.I. Cade, T. Ritman-Meer, D. Richards, Phy. Rev. B 79 (2009) 241404–241407.